*Desalination and Water Treatment*
www.deswater.com
doi: 10.5004/dwt.2020.25570

189 (2020) 227–242
June

# Highly porous iron-zirconium binary oxide for efficient removal of Congo red from water

Jhilirani Mohanta[a], Banashree Dey[b], Soumen Dey[a,*]

[a]*Department of Chemistry, Central University of Jharkhand, Ratu-Lohardaga Road, Brambe, Ranchi-835205, Jharkhand, India, Tel. +91-9661399711; email: soumen.dey@cuj.ac.in (S. Dey)*
[b]*Department of Chemistry, The Graduate School College for Women Jamshedpur, Sakchi, Jamshedpur-831001, Jharkhand, India*

Received 18 June 2019; Accepted 3 February 2020

**ABSTRACT**

Wastewater from textiles and other industries containing dyes pose a serious health hazard. To address the issue, the present study reports the removal of a toxic Congo red (CR) from water by a non-toxic iron-zirconium mixed binary metal oxide (IZO) as adsorbent. The material was prepared by a controlled co-precipitation method under mild basic condition and isolated in an 85% yield. It was characterized using Fourier-transform infrared spectroscopy (FTIR), scanning electron microscopy, Brunauer–Emmett–Teller (BET) surface area and powder X-ray diffraction. High BET surface area (200.307 $m^2$ $g^{-1}$) supports an excellent adsorption capacity of 171 mg $g^{-1}$ at pH 6. FTIR shows the presence of hydroxyl moieties along with surface water. The influence of adsorbent dose, contact time, pH, agitation speed, temperature, and concentration were optimized. The adsorption follows pseudo-second-order kinetics ($R^2$ = 0.998) and is best described by the Langmuir isotherm model ($R^2$ = 0.988). Negative free energy change suggests a spontaneous process. Co-existent ions impart moderate competitive inhibition to the adsorption process. 78% regeneration was achieved with sodium hydroxide solution. IZO retains its efficiency up to five cycles. Designed column experiments show that under the optimized condition of a column comprised of 4 cm bed height, 2 L dye discoloration was successful. The breakthrough was analyzed by Thomas, Yoon–Nelson, and Adams–Bohart model. Column run follows Thomas and Adams–Bohart model. High application potential, low cost, and reusability of the IZO make it a promising adsorbent for the removal of CR from contaminated water.

*Keywords:* Congo red; Binary oxide; IZO; Adsorption; Regeneration; Breakthrough

## 1. Introduction

The scarcity of drinking water due to the rapid growth of population and increased industrialization is of major concern these days [1]. Dyes are used in industries including but not limited to textile, paint and pigment, food and beverage, plastic, paper, cosmetics and pharmaceuticals [2–4]. Effluent from different industries causes several diseases such as organ damage, hemolysis, respiratory disorders, hypertension, etc. [5]. Dye contaminated water slows down photosynthesis, hinders solar light penetration and stops re-oxygenation capacity, thereby affecting the aesthetic of water resources [6,7]. Industrial discharge without proper treatment causes irreparable damage to the crops and living beings, both aquatic and terrestrial [8]. Dyes are highly water-soluble, toxic in nature, chemically stable to biodegradation and photo-degradation [9,10]. Congo red (CR) is well-known to cause an allergic reaction and to metabolize to benzidine, a human carcinogen [11]. Thus, need has emerged to remove such dyes from contaminated water. Removal of dyes from contaminated effluent is mainly categorized into three methods: physical, biological and chemical methods. These methods include photo-catalysis, anaerobic treatment, membrane filtration, coagulation, oxidation, biosorption, and adsorption. Among all the methods, the physical method

* Corresponding author.

is easier and cost-effective; the adsorption process belongs to this method [12–15].

Various types of adsorbents (chemisorbent and biosorbent) and ion exchangers are developed for the removal of dyes. Biosorbents from agricultural and forestry waste materials were used for large scale dye removal due to their low cost and availability. Several researchers have introduced different low-cost bio-sorbent such as different tree bark powder, coconut shell activated carbon, cellulose, raw pine, and acid-treated pine cone, mahua seed, wheat shells, and bagasse, etc. These low-cost biosorbents were used extensively for dye removal from wastewater [16–18]. Macroalgae were also used as promising bio-sorbent [19].

Recently, clay is being used as a low-cost adsorbent, which is naturally available and is environmentally friendly in nature. Non-toxic nature and high surface areas are favorable for the removal of dyes from effluents. Acid modified clay enhances the rate of adsorption, porosity and surface area [20–25].

Lignin and its derivatives used as scavenger intended for its structural complexity bearing hydroxyl, carbonyl, carboxyl, and other active groups enhance the adsorption capacity [26,27]. Polymeric, metal coordinated xerogel was investigated for the elimination of wastewater containing sulfonic dyes. Heterocyclic thiadiazole compounds make available excellent binding sites to form coordination complexes with Cu(I), Cu(II), Zn(II), which demonstrate as a good adsorbent [28]. Cellulose advances its adsorption capacity after chemical modification as a result of preamble functional groups on the surface [29]. It has been shown that weakly and strongly basic anion exchanger resins exhibit good adsorption properties. Researchers had used polystyrene-based anion exchanger resin amberlite IRA-938 for the removal of rose bengal dyes from aqueous solutions [30].

Recently $Fe_3O_4$-bis(trimethoxysilylpropyl) amine was tested for dye adsorption, and the mechanism showed that electrostatic force of attraction and hydrogen bonding are driving force for the interaction [31]. $TiO_2$ nanoporous electrode was used for dye adsorption in a fabricated process by dye-sensitized solar cells [32]. Copper complexes were synthesized which have attractive architectures and potential applications in adsorption [33]. Currently, different metal oxides, mixed metal oxides, and their composites are in use for removal of contaminants from wastewater [34–37].

Metal-organic frameworks have attracted attention because of its properties like ultra-high surface area, surface charge, tunable pore, and are applicable in adsorption of dyes. Hydrophobic interactions, $\pi-\pi$ interaction and electrostatic attraction govern the adsorption process. Zeolitic imidazole framework has excellent chemical and thermal stability properties showing the adsorption of dyes from aqueous solution [38]. Carbon nanotube-based magnetic hybrids were used as an adsorbent. It has good magnetic properties, dispersibility, and tremendous adsorption capacity. The magnetic graphene and magnetic carbon nanotube achieve adsorption of dyes from contaminated water [39]. Spinel like $Co_3O_4/TiO_2$/GO and a composite material of $TiO_2$ and alum sludge photo-catalytically degrade toxic organic compounds from water [40,41]. Adsorption properties of ZnS/SnS/A-FA [42] and $LaFeO_3$ doped mesoporous silica shows a unique fine pore, in this pore large organic molecule, are transported and reach the active site for catalytic degradation and adsorption [43]. Researchers developed a nanostructure $TiO_2/SnO_2$ binary metal oxide for photolytic degradation of dye [44]. Metal oxide and mixed metal oxides are also used as adsorbent [45]. High adsorption capacity is shown in the zirconium composite [46]. Currently, cadmium oxide, guar gum/copper oxide, trimetallic composite, and cobalt-zinc ferrite have been explored by Pathania et al. [47,48], Sharma et al. [47,48], and Tatarchuk et al. [49,50] for removal of dyes and heavy metals from the aqueous phase [51]. Karthik et al. [52] and Mironyuk et al. [53–55] have synthesized NiO nanoparticle, mesoporous titania for removal of pollutants from contaminated water [56].

Ternary metal oxide adsorbent brought high surface area, availability of active atom on the surface of metal oxide adsorbent, high stability and regeneration capacity [57]. We have recently demonstrated the removal of methylene blue using a composite material made up of metal oxide fabricated ethylene diamine composite [58].

The present work reports the synthesis of iron-zirconium mixed metal oxide by the co-precipitation method as a scavenger of CR. Batch, adsorption kinetics, isotherm, thermodynamics, and fixed-bed column studies were conducted to get a comprehensive idea of the dye uptake.

## 2. Experimental section

### 2.1. Materials and methods

Analytical grade reagents were used for all work. Solutions were prepared in double distilled water. Zirconyl oxychloride ($ZrOCl_2{\cdot}8H_2O$, Spectrochem, Mumbai, India), ferric chloride ($FeCl_3{\cdot}4H_2O$, Merck, Mumbai, India), hydrochloric acid ammonia (Fischer Scientific, Mumbai, India) was used as received. CR was purchased from Merck (Mumbai, India). The absorbance of solutions was recorded in a Hitachi double beam UV-Vis spectrophotometer (model U-2900, Japan) at 494 nm. UV-solution program was used to calculate concentrations. Fourier-transform infrared spectroscopy (FTIR) spectra were analyzed in a Perkin Elmer spectrophotometer (model spectrum II, Massachusetts, USA). Morphological analysis was carried using scanning electron microscopy (SEM) in a Jeol JSM-6390LV (Tokyo, Japan). Powder X-ray diffraction (XRD) pattern was determined in AXRD proto benchtop. Rotary orbital shaker (Sohag, New Delhi, India) was used for all batch experiments. The pH of solutions was carried out with the help of pH meter (Systronics, Kolkata, India). Remi-bench top centrifuge (R-8 M, Kolkata, India) was used for centrifugation.

### 2.2. Synthesis of binary metal oxide (IZO)

The mixed binary oxide was synthesized through the co-precipitation method. 3.22 g (0.1 M) zirconyl oxychloride octahydrate and 1.62 g (0.1 M) ferric chloride tetrahydrate was separately dissolved into 100 mL HCl solution. Both were then mixed with continuous stirring. 0.5 M $NH_4OH$ was added dropwise till the pH reached 6 and stirred continuously for 3 h. The resulting dark brown precipitate was left overnight for aging. The precipitate was filtered and washed with water several times to remove the untreated substances

and was dried in an oven at 65°C for 20 h. The IZO binary oxide adsorbent thus obtained was cooled, ground and sieved (80–160 mesh). Finally, the adsorbent was preserved in desiccators for further use. Scheme 1 outlines synthesis, batch run, and regeneration.

IZO was characterized by $pH_{zpc}$, FTIR, SEM, powder XRD and thermogravimetric analysis (TGA).

### 2.3. Batch adsorption experiments

The adsorption experiments were performed in an orbital shaker in batch mode. The stock solution of 1,000 mg $L^{-1}$ CR was prepared in de-ionized water and used further to prepare solutions of desired strength. All results are an average of five sets.

In each experimental setup, 0.05 g IZO was added to 50 mL of 10 mg $L^{-1}$ CR solution in LDPE bottles. The optimum pH was set and shaken at 120 ± 5 rpm for 120 min to find out the equilibrium time of adsorption. The solution was then centrifuged at 5,000 rpm for 5 min. Absorbance was recorded in a UV-vis spectrophotometer. Percentage adsorption and adsorption capacity was determined using Eqs. (1) and (2), respectively.

$$E\% = \frac{\left(C_0 - C_e\right)}{C_0} \times 100 \tag{1}$$

$$q_e = \left(C_0 - C_e\right) \times \frac{V}{m} \tag{2}$$

where $E\%$ = adsorption percentage, $q_e$ = adsorption capacity at equilibrium (mg $g^{-1}$), $C_0$ and $C_e$ are initial and final concentrations (mg $L^{-1}$) respectively, $V$ is the volume (mL) of solution taken and $m$ (g) is the weight of adsorbent used.

Optimization of physicochemical parameters such as contact time, pH, initial concentration of dye, temperature, and adsorbent dose was done systematically.

The zero point charge of the adsorbent was measured by the pH drift method as follows: 500 ml of 0.01 M NaCl stock solution was prepared; 100 mg of IZO was added to 50 mL NaCl solution, with pH range 2–11. After shaking for 24 h at 120 ± 5 rpm at room temperature the final pH of the NaCl solution was measured and was plotted against the initial pH. At a particular pH, the surface becomes neutral. Evaluated pHzpc was found to be 6.66. The behavior of adsorbent over a pH range can be explained by a zero-point charge.

Five solutions were prepared with an optimized pH of 5, 6, 7, 8 and 9 by adding 0.1 N HCl and 0.1 N NaOH. 0.05 g of IZO adsorbent was added to each bottle and kept in a shaker at room temperature at 120 ± 5 rpm for 40 min. The solutions were centrifuged and analyzed in a UV-Visible spectrophotometer to compare the effect.

For the kinetic study, 50 ml of 10mg $L^{-1}$ CR solution of pH 6 were taken and 0.05 g of IZO was added to it. The solution was shaken in an orbital shaker for 30 min with a shaking speed of 120 ± 5 rpm. Aliquots were taken out at different time intervals of 3, 6, 9, 12, 15, 20, 25, and 30 min. Residual concentrations were measured and results were interpreted with various kinetic models (results and discussion section).

For isotherm study; CR (50 mL) of different concentrations of 2.5, 5, 7.5, 10, 12.5, and 15 mg $L^{-1}$ were prepared from the stock solution and pH was adjusted to 6. 0.05 g of IZO adsorbent was added, shaken for 2 h. at 288, 298, and 308 K. Final concentrations were measured. Results were analyzed by Langmuir and Freundlich adsorption isotherms.

All thermodynamic parameters were evaluated as follows: CR solution of a concentration of 5, 10, and 15 mg $L^{-1}$ was prepared from the stock solution. Each 50 ml solution was adjusted at pH 6. 0.05 g of IZO was added and was shaken for 2 h at 288, 298, and 308K. Final concentrations were evaluated and analyzed with various models. Van't Hoff plot was made.

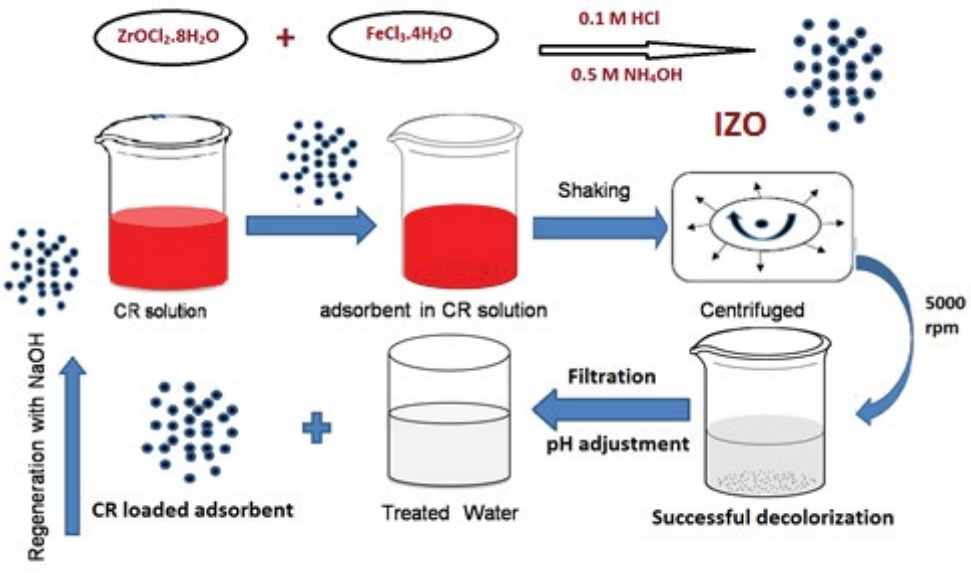


Scheme 1. Synthesis of IZO, adsorption pathway and regeneration

Dose variation was done as follows: 10 mg $L^{-1}$ solution of CR was set at pH 6. To it, 0.05, 0.1, 0.15, 0.2, 0.25, and 0.30 g IZO was added and agitated for 40 min at shaking speed of 110 ± 5 rpm. Final concentrations were measured.

For the input concentration effect, CR solutions (2.5, 5, 7.5, and 10 mg $L^{-1}$) were prepared from the stock solution. pH 6 was maintained; 0.05 g of IZO was added. After shaking under optimized conditions, residual concentrations were measured.

For interference test following concentrations were used to prepare model contaminated water: nitrate (5 mg $L^{-1}$), chloride (200 g $L^{-1}$), sulfate (200 mg $L^{-1}$) and arsenate (0.05 mg $L^{-1}$).

Regeneration and recovery were done as follows: After the batch experiment, dye loaded IZO was washed thoroughly with distilled water to remove adhering surface dyes, dried at 80°C and treated with the three different solutions namely 0.3 M of NaCl, NaOH and HCl solution for 5 h. Finally, solutions were centrifuged and leached dye concentration was measured and percentage regeneration was calculated. Regenerated material was neutralized with dilute hydrochloric acid till pH 6.5 was attained. Further experiments for cycle efficiency were carried out. The leached dye was stored.

Continuous flow breakthrough experiments were executed in a fixed bed glass column of 50 cm height and 0.85 cm internal diameter. Bed height was suitably adjusted by varying amounts of IZO. The known CR solution was pumped to the column in a down-flow by flow rate 6, 8, and 12 ml $min^{-1}$. The effluents were collected in regular intervals and concentrations were measured.

Bed height of 3.2, 4.8 and 6.3 cm was varied with different influent concentrations 1, 5, and 10mg $L^{-1}$ at different pH 5, 6, 7, 8 and 9, respectively.

The maximum adsorption coefficient was estimated as follows: 50 mL of CR (500 mg $L^{-1}$) was agitated with 0.5 g IZO under optimized condition. From residual concentration, the maximum adsorption capacity was estimated to be 171 mg $g^{-1}$.

## 3. Results and discussions

### 3.1. Characterization of adsorbent

#### 3.1.1. Fourier-transform infrared spectroscopy

FTIR spectra were recorded in the range 4,000–400$cm^{-1}$. The broad peak appeared at 3,381 $cm^{-1}$ for free IZO. This is due to the O–H stretching. Upon adsorption, this peak was found to get shifted to 3,356 $cm^{-1}$. Such a lowering of frequency confirms the interaction of IZO with CR. It is consistent with earlier reports [59]. The peak at 1,630 $cm^{-1}$ is due to the bending vibration of O–H. The vibrational frequency corresponding to tetrahedral and octahedral cations of M–O bond were present in the range 550–600 $cm^{-1}$ and 390–400 $cm^{-1}$ respectively [58]. The peak at 693 and 490 $cm^{-1}$ represent Zr–O and Fe–O stretching [60]. Upon adsorption, peak at 490 $cm^{-1}$ gets shifted to 479 $cm^{-1}$ due to the formation of weak hydrogen bonding between IZO and CR. Moreover, new peaks were found to appear at 2,800; 1,122; and 990 $cm^{-1}$ after dye adsorption. This indicates the presence of CR in loaded material. Weak bands around 2,800 $cm^{-1}$ represent aromatic C–H stretching originating from phenyl groups of CR. The peak at 1,122 $cm^{-1}$ represents C–N stretch. The peak at 990 $cm^{-1}$ represents C–H bending. Comparative FTIR of pure IZO and dye loaded one is presented in Fig. 1.

#### 3.1.2. Scanning electron microscopy

SEM images of IZO (Fig. 2) represents that the adsorbent is porous in nature. The particles are heterogeneous, irregular in shape and found mostly in the micrometer range. Considerable numbers of pores can be seen. The IZO materials have pores on the surface having a large surface area. According to the surface of the volume ratio, there is a large surface for the adsorption of CR due to the porous surface area [19]. No significant changes were seen upon dye loading except the reduction of pores.

#### 3.1.3. X-ray diffraction

Crystallinity and presence of various components can be assessed by powder XRD. Fig. 3 shows powder XRD of IZO. Notable peaks at 18° and 24° represents the presence of $ZrO_2$ and $Fe_2O_3$ units (JCPDS card numbers: 81-1551, 39-1346) [61]. The material is micro-crystalline in nature. This is helpful in the column run since the problem of leaching out is minimized.

#### 3.1.4. Thermogravimetric analysis

The thermal stability of the adsorbent was tested by TGA. It was observed that up to 80°, no decomposition takes place, which indicates the amiable stability of the adsorbent (Fig. 4). Further, a mass loss of 20% was observed, which may be attributed to the removal of surface water from the mixed metal oxide. However, this mass loss is attributed to the loss of physically adsorbed water [51,56]. The weight loss of IZO and the destruction of IZO materials was studied in the temperature range from 30°C to 320°C. The second mass loss at

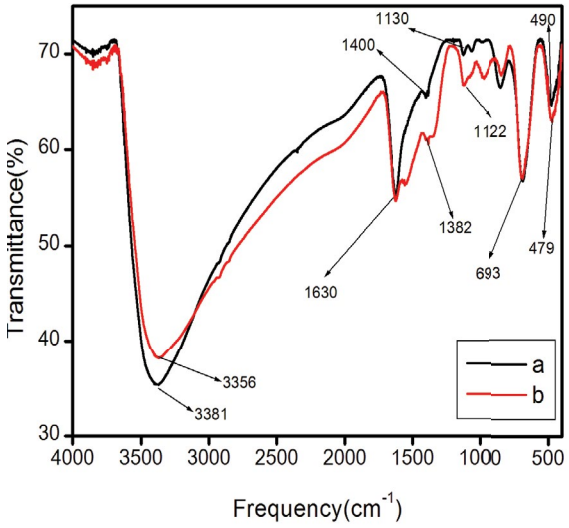


Fig. 1. FTIR spectra of IZO; (a) before and (b) after adsorption of CR.

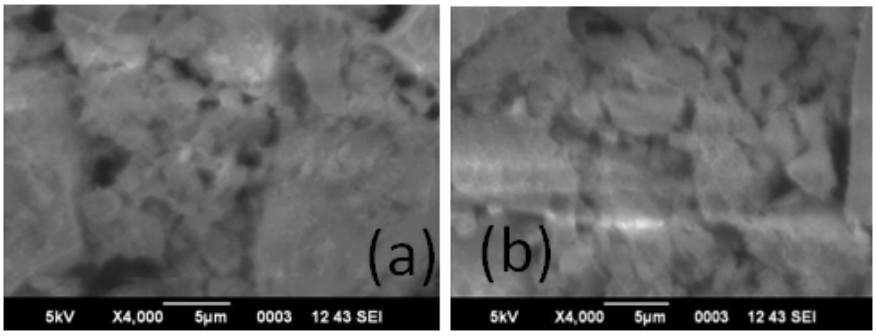


Fig. 2. SEM images of the adsorbent (a) before and (b) after adsorption.

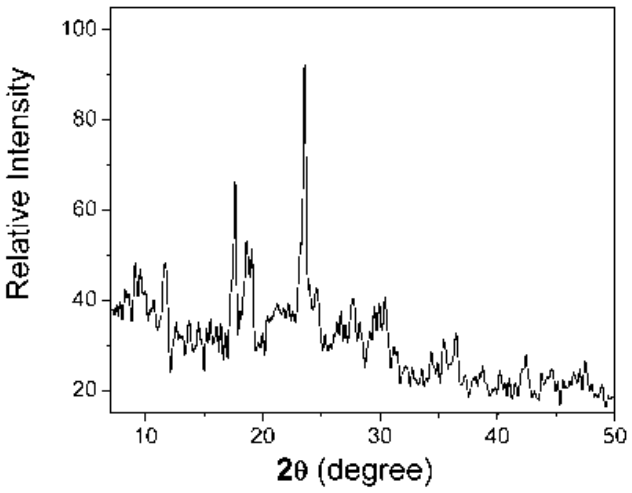


Fig. 3. Powder XRD pattern of the adsorbent.

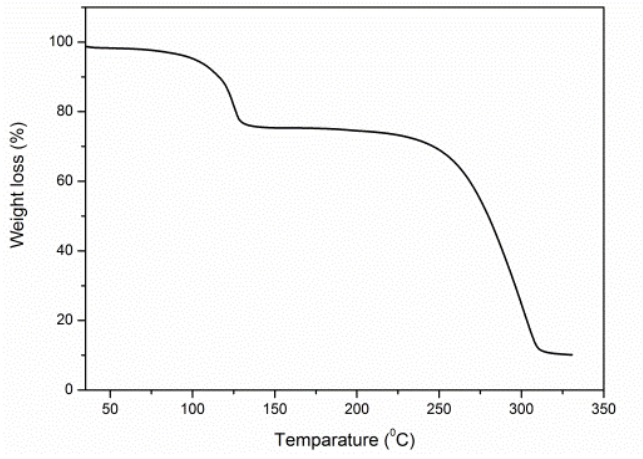


Fig. 4. TGA plot of the adsorbent.

a higher temperature may be due to loss of all bound water molecules and partial decomposition of the material [26].

### 3.1.5. Zero-point charge ($pH_{zpc}$) and effect of pH

Adsorption is a pH dependent phenomenon and zero-point charge helps in predicting precise mechanisms at

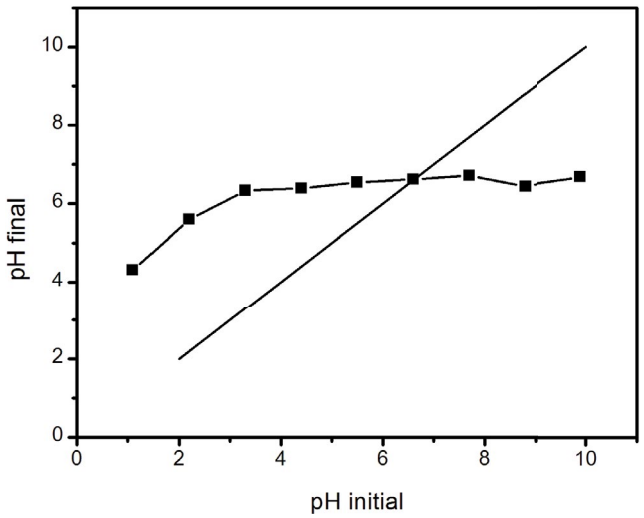


Fig. 5. Determination of zero point charge ($pH_{zpc}$) of IZO.

various pH. Net surface charges are a useful parameter to estimate the nature of active centers on the adsorbent surface. When pH > $pH_{zpc}$, the adsorbent surface is negatively charged, which results in deprotonation. The surface becomes negatively charged. When pH < $pH_{zpc}$, the adsorbent surface is positively charged. In that case, electrostatic interaction prevails. In the present case, pH < $pH_{zpc}$, so IZO possesses a positively charged surface at working pH 6 (Fig. 5). Both cases are presented schematically below.

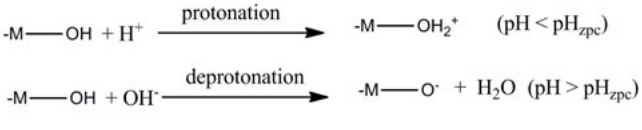


### 3.2. Batch experiments

#### 3.2.1. Effect of pH

Solution pH is a very important factor for adsorption to take place. pH from 5–9 were tested to identify optimum one. It was seen that the removal efficiency is reasonably high at lower pH and decreases steadily with an increase in pH (Fig. 6b). At lower pH, the surface of the

IZO particles becomes positively charged. Also, the concentration of $H^+$ ion in solution is pretty high. The favorable electrostatic attraction with anionic CR accounts for high removal [26]. At high pH, the presence of a high concentration of hydroxyl ions increases the negative charge on the IZO surface by deprotonation of the positively charged sites. Electrostatic repulsion with CR leads to a decrease in the adsorption [14,15]. In addition, an increased number of hydroxyl ions induces competitive inhibition with CR, thereby further decreasing adsorption efficiency. It is noteworthy that CR gradually changes color below pH 5, hence not studied.

Solution pH determines the degree of electrostatic interaction between the adsorbent and adsorbate charge distribution on the materials [3–5,27]. The zero point charge of IZO was found to be 6.60. That means $pH_{working} < pH_{zpc.}$

### 3.2.2. Effect of contact time

Equilibration time was estimated by varying contact time. The rate of adsorption was seen to be very high initially which became constant after 40 min (Fig. 6a). This can be explained by the fact that initially, the numbers of available pores are very large which allows adsorption to take place easily. With time, available active sites got saturated and no significant adsorption took place. Moreover, intermolecular repulsion between negatively charged CR molecules hinders further uptake onto the IZO surface. This is consistent with earlier observations [18,23–25,27].

### 3.2.3. Effect of initial dye concentration

The effect of initial dye concentration is given in Fig. 6c. With the increase in dye loading concentration, percentage adsorption decreases. This could be attributed to the fact that at a lower concentration of dye, there is a high driving force for mass transfer on the adsorbent surface [18,28]. Also, at a low dye/adsorbent ratio, higher sorption sites are available. Upon increasing ratio, active sites get saturated and the adsorbent surface becomes surrounded with a higher number of dye molecules. Repulsive interaction is responsible for reduced uptake [16].

### 3.2.4. Effect of adsorbent dose

The variation of the adsorbent dose is shown in Fig. 6d. The removal efficiency steadily increases with increasing dose. This is due to the availability of exchangeable sites at the surface [26].

### 3.2.5. Effect of interference

Commonly nitrate, sulfate, phosphate, chloride, arsenate and carbonate ions are present in groundwater. Wastewater from different industries contains co-existent ions. Interference was checked with maximum permissible concentrations of chloride, nitrate, phosphate, sulfate and arsenate. Approximately 20% decrease in dye uptake was noticed suggesting a strong inhibition. (Fig. 6e)

## 3.3. Kinetics studies

Adsorption kinetics gives an idea of adsorbent–adsorbate interaction, precisely the nature of the mechanism [17,27].

Adsorption kinetics for pseudo-first-order [Eq. (3)], pseudo-second-order [Eq. (4)], intra particle [Eq. (5)] and second-order [Eq. (6)] were analyzed.

$$\ln\left(q_e - q_t\right) = \ln q_e - k_1 t \tag{3}$$

$$\frac{t}{q_t} = \frac{1}{\left(k_2 \cdot q_{e^2}\right)} + \frac{t}{q_e} \tag{4}$$

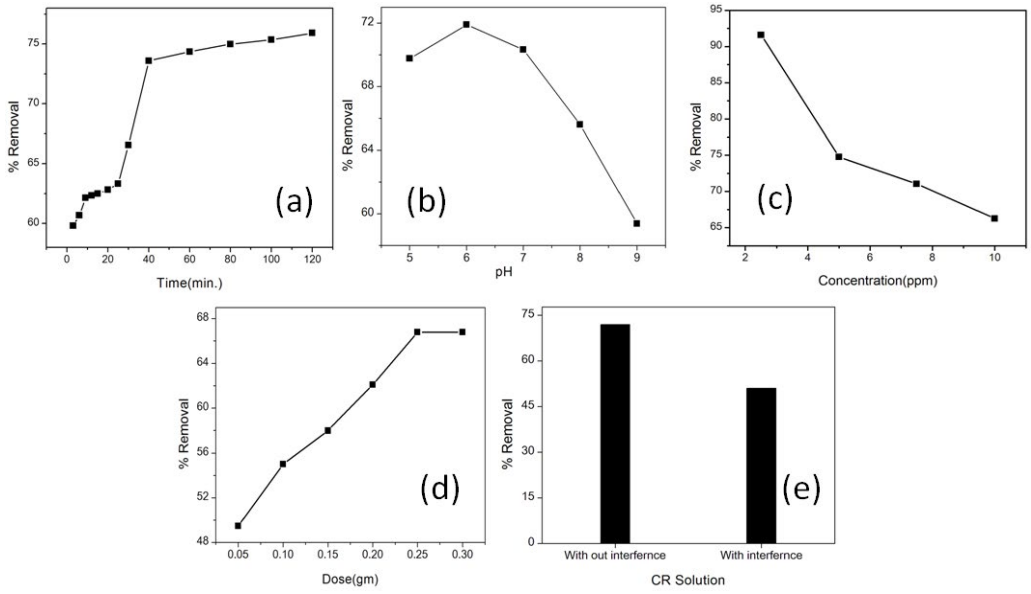


Fig. 6. (a) Effect of contact time on adsorption, (b) Effect of pH on adsorption, (c) Effect of input concentration on the removal of Congo red by IZO adsorbent, (d) Effect of adsorbent dose on adsorption, and (e) Effect of interference on dyes uptake.

$$q_t = k_{id} t^{0.5} + C \quad (5)$$

$$\frac{1}{(q_e - q_t)} = \frac{1}{q_e} + k_t \cdot t \quad (6)$$

where $q_e$ and $q_t$ (mg g$^{-1}$) are the amount of CR adsorbed at equilibrium and at time $t$ (min) respectively; $k_1$ (min$^{-1}$), $k_2$ (g mg min$^{-1}$), $k_{id}$ (mg g min$^{0.5}$), $k_t$ are rate constant of pseudo-first-order, pseudo-second-order, intraparticle diffusion and second-order, respectively.

It is known that adsorbate transport from bulk solution into the solid adsorbent phase goes through an intra-particle diffusion process, which is a predominately rate-limiting step [14]. The pseudo-second-order model was found to be the best fit ($R^2$ = 0.998) (Fig. 7a and Table 1). This indicates that adsorption is predominantly chemisorptions. Non zero value of $K$ and high value of $q_e$ in intraparticle diffusion suggests that the rate-controlling step is chemical adsorption [17,26]. Boundary layer thickness also plays an important role in the mass transfer process. Relevant kinetic parameters are summarized in Table 1.

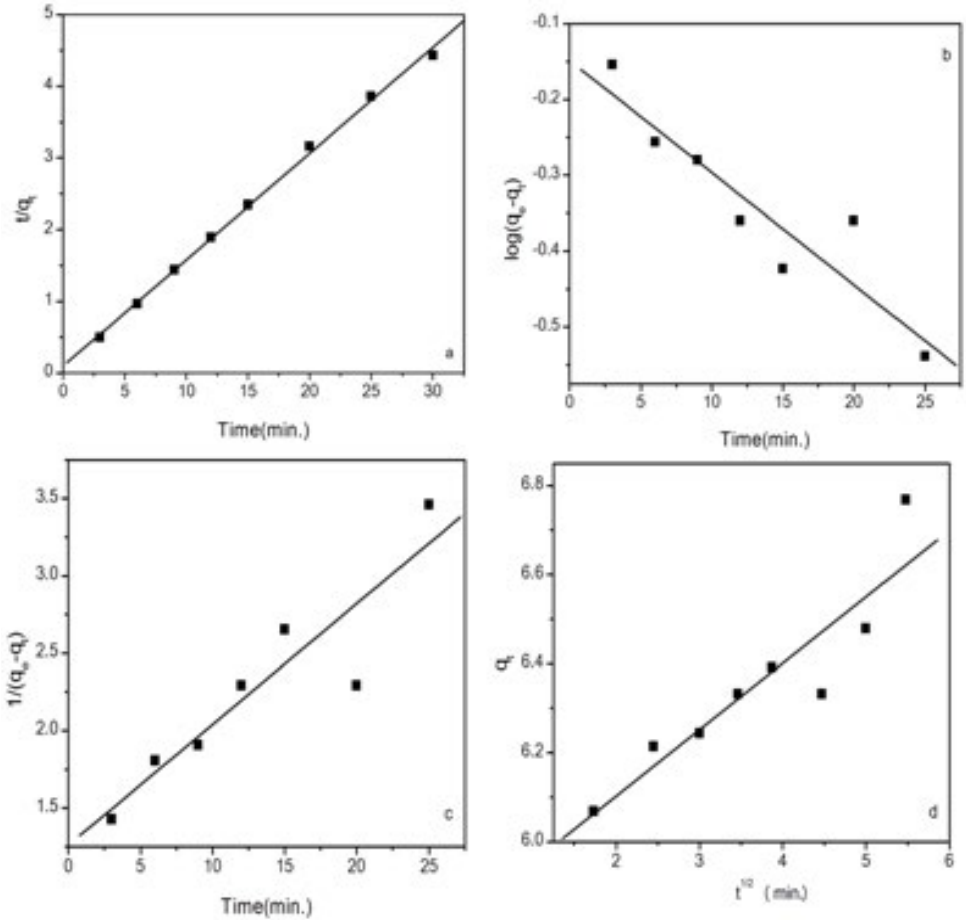


Fig. 7. Kinetic models of CR adsorption by IZO (a) pseudo-second-order, (b) pseudo-first-order, (c) second-order, and (d) intraparticle diffusion.

Table 1
Calculated kinetics models constant

| Order | $q_e$ (mg g$^{-1}$)[a] | $K$[b] | $R^2$[c] |
|---|---|---|---|
| Pseudo-first-order | 0.6881 | 0.036 min$^{-1}$ | 0.844 |
| Pseudo-second-order | 6.845 | 0.2193 mg g$^{-1}$ min$^{-1}$ | 0.998 |
| Second-order | 0.7936 | 0.07799 mg g$^{-1}$ min$^{-1}$ | 0.842 |
| Intraparticle diffusion | 5.804 | 0.14908 mg g$^{-1}$ min$^{-0.5}$ | 0.840 |

[a]Equilibrium CR uptake/g of adsorbent
[b]Kinetic constants
[c]Correlation coefficient

### 3.4. Adsorption isotherms

The study of isotherm models reveals a possible mode of interaction of the dye with the adsorbent surface as a function of concentration at a particular temperature. Langmuir and Freundlich models were studied Eqs. (7) and (8).

$$\frac{C_e}{q_e} = \frac{1}{Kq_{\max}} + \frac{C_e}{q_{\max}} \tag{7}$$

$$\ln q_e = \frac{1}{n}\ln C_e + \ln K_f \tag{8}$$

where $C_e$ (mg L$^{-1}$) is the equilibrium concentration, $q_e$ (mg g$^{-1}$) is the amount adsorption per unit mass of the adsorbent, $q_{\max}$ (mg g$^{-1}$) is the maximum amount of adsorbate adsorbed per unit mass, $K$ is the Langmuir affinity constant (L g$^{-1}$). $q_{\max}$ and $K$ were estimated from the slope and intercept of linear plot $C_e$ against $C_e/q_e$, where $q_e$ (mg g$^{-1}$) is the amount of CR adsorbed per unit weight at equilibrium, $C_e$ (mg L$^{-1}$) is the equilibrium concentration of the CR solution, $K_f$ is the constant related to the adsorption capacity of the adsorbent. $1/n$ is the constant related to the adsorption intensity of the adsorbent.

Adsorption isotherms were studied at 288, 298, and 308 K and presented in Fig. 8. Corresponding isotherm parameters ($b$, $q_{max}$, $K_f$, and $n$) are given in Table 2. Langmuir model assumes monolayer adsorption onto a homogeneous surface without any lateral interaction [14,19]. Freundlich models suggest the heterogeneous interaction in between the adsorbent and adsorbate [11–13,17]. In the present case, the Langmuir model was found to fit well ($q_e$ = 11.93 mg g$^{-1}$, $R^2$ = 0.988) which suggests homogeneous interaction between the dye molecules and the IZO surface takes place.

### 3.5. Thermodynamics studies

Thermodynamics parameters are essential for understanding the relation between adsorbate and adsorbent. Gibbs free energy ($\Delta G$, kJ mol$^{-1}$), entropy ($\Delta S$, kJ mol$^{-1}$) and enthalpy ($\Delta H$, kJ mol$^{-1}$) were estimated from the following equation [Eqs. (9)–(12)]. $\Delta S$ and $\Delta H$ are calculated using van't Hoff linear regression analysis [ln (55.5 $K_d$) vs. $1/T$] (Fig. 9) [55]. Enthalpy and entropy were calculated from the slope and intercept, respectively.

$$\ln\left(55.5K_d\right) = \frac{\Delta S}{R} - \frac{\Delta H}{R}\cdot\frac{1}{T} \tag{9}$$

$$\Delta G = \Delta H - T\Delta S \tag{10}$$

$$\Delta G = -RT\ln\left(55.5K_d\right) \tag{11}$$

$$K_d = \frac{q_e}{C_e} \tag{12}$$

where $R$ stands for universal gas constant and $K_d$ is the ratio of equilibrium uptake to concentration.

Thermodynamics studies provide important information about the adsorption process, its feasibility, spontaneity and randomness/chaos at the sorbate-sorbent junction. It was observed that the adsorption favors at a lower temperature. For an exothermic process, van't Hoff plot should have a positive slope, $\Delta H < 0$, so $-\Delta H/R > 0$. Negative enthalpy change ($\Delta H$) indicates that the process is exothermic; therefore lower temperature promotes adsorption. Also, negative entropy change ($\Delta S$) indicates decreased randomness of the solute solution interface during the adsorption process [62].

Table 2
Selected isotherm parameters

| Isotherm models | $T$(K) | $T$(K) | $T$(K) |
|---|---|---|---|
| Langmuir | 288 | 298 | 308 |
| $K$ (L mg$^{-1}$)[a] | 1.030 | 0.337 | 1.07 |
| $q_0$ (mg g$^{-1}$)[b] | 11.24 | 11.93 | 11.35 |
| $R^2$[c] | 0.980 | 0.988 | 0.980 |
| Freundlich | 288 | 298 | 308 |
| $K_f$ (mg g$^{-1}$)[d] | 2.175 | 2.884 | 2.129 |
| $n$[e] | 1.241 | 1.479 | 1.990 |
| $R^2$[c] | 0.936 | 0.986 | 0.983 |

[a]Langmuir constant related to sorption energy, L mg$^{-1}$
[b]Maximum adsorption capacity, mg g$^{-1}$
[c]Correlation coefficient
[d]Freundlich constant related to adsorption, mg g$^{-1}$
[e]Freundlich constant

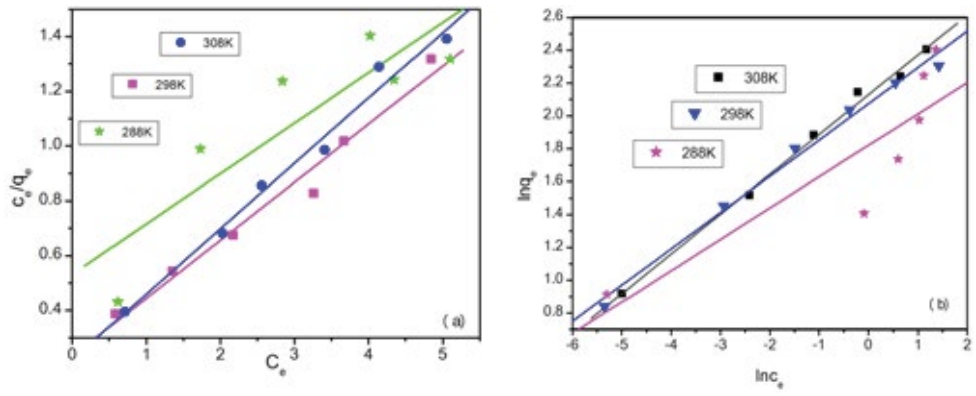


Fig. 8. Isotherm models: (a) Langmuir model and (b) Freundlich model.

Considering adsorption to be a complex process, reduced adsorption at high temperatures might be due to the small amount of desorption. Selected thermodynamic parameters are given (Table 3).

### 3.6. Regeneration study

The desorption process helps to understand the mechanisms of adsorption and the scope of recovery of the adsorbate as well as the adsorbent. 78% of regeneration was achieved with 0.3 M NaOH. Regeneration percentage was calculated using the Eq. (13):

$$R\% = \frac{C_t}{C_0} \times 100 \tag{13}$$

where $C_0$ and $C_t$ are concentration before and after adsorption, respectively. Cycle efficiency was measured and presented in Fig. 10.

### 3.7. Column study

Fixed bed column experiments were carried out to investigate the dynamic adsorption properties of IZO. After obtaining promising results from batch experiments, bench-scale column studies were performed by varying pH, input concentration, dose, and interference. For a model experiment, 4 g adsorbent was used to make the bed height of 3 cm in a glass column having an internal diameter of 0.85 cm.

Fig. 11a–e shows the effects of various parameters in column run and selected column parameters are shown in Tables 4–6. Four fixed-bed column experiments were performed by varying concentration, pH, dose and interference. The internal diameter of the column is 0.85 cm. 1, 5, and 10 mg $L^{-1}$ dye solutions were prepared for concentration variation. Different pH solutions of CR from 5–9 were used for a fixed-bed column study. The treated runoff was collected in a certain time interval. The bed volume was calculated (1 BV = $\pi r^2 h$) (Tables 4–6). After the first column run, the adsorbent was regenerated and reused for five cycles. Increasing concentration decreases dye uptake (Fig. 11b).

The change in pH affected the saturation rate and adsorption capacity of the dye (Fig. 11a). Fig. 11c shows the effect of varying doses on adsorption. It gives consistent results as batch experiments. Moderate interference was noticed in the column (Fig. 11d). The effect of the flow rate was presented in Fig. 11e.

### 3.8. Breakthrough study

Breakthrough studies were conducted to ascertain the column behavior of dye in a fixed bed.

With increasing pH, the highest result was obtained at pH 6 followed by a decrease (Fig. 12a). This is because at pH 6, the surface of IZO contains a large no of active sites [63].

Three different flow rates of 12, 8, and 6 ml $min^{-1}$ were chosen for the estimation of a breakthrough. A higher flow

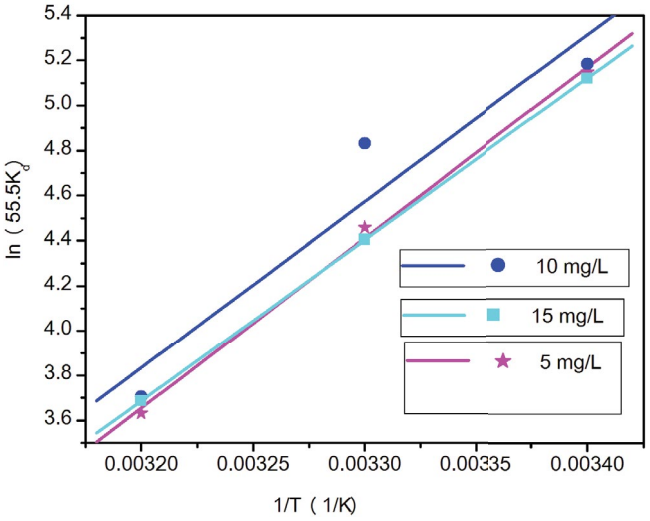


Fig. 9. Van't Hoff plot.

Table 3
Thermodynamics parameters for CR adsorption

| Concentration (mg $L^{-1}$)[a] | $T$(K)[b] | $\Delta G$ (J $mol^{-1}$)[c] | $\Delta H$ (J $mol^{-1}$)[d] | $\Delta S$ (J $mol^{-1}$ $K^{-1}$)0[e] |
|---|---|---|---|---|
| 5 | 288 | –13.312 | –46.3922 | –0.114 |
| | 298 | –12.402 | | |
| | 308 | –11.259 | | |
| 10 | 288 | –11.885 | –38.825 | –0.095 |
| | 298 | –11.746 | | |
| | 308 | –10.319 | | |
| 15 | 288 | –12.259 | –59.611 | –0.164 |
| | 298 | –11.457 | | |
| | 308 | –9.438 | | |

[a]Concentration of CR mg $L^{-1}$
[b]Temperature in K
[c]Change in Gibbs free energy
[d]Change in enthalpy
[e]Change in entropy

rate leads to a faster saturation leading to an early breakthrough (Fig. 12b). Such events are found consistent with reported ones [64]. The effect of concentration is presented in Fig. 12c.

To know the effect of bed height on breakthrough, three different heights 3.2, 4.8 and 6.3 cm were chosen. As the bed height increases the dye solutions have more contact with the adsorbent leading to higher dye removal (Fig. 12d) [65].

The successful design of a column adsorption requires the prediction of a concentration-time profile. In order to explain fixed-bed column behavior Thomas, Yoon–Nelson and Adams–Bohart models were tested using Eqs. (14)–(16) [66].

$$\ln\left(\frac{C_0}{C_t}-1\right)=\frac{K_{TH}q_0m}{Q}-K_{TH}C_0t \tag{14}$$

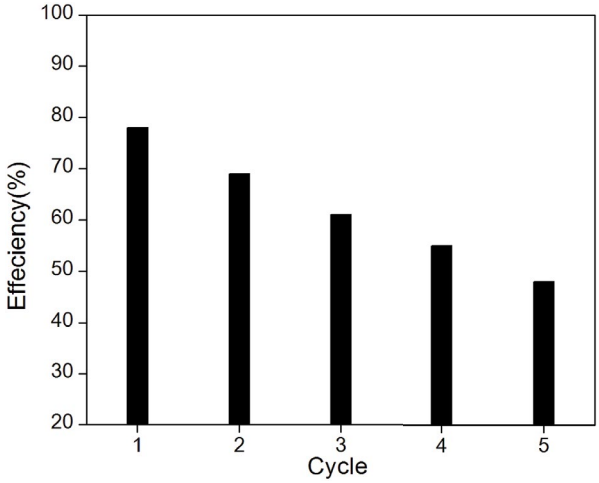


Fig. 10. Cycle efficiency of IZO.

where $K_{TH}$ is the Thomas kinetics coefficient (mL min$^{-1}$ mg$^{-1}$), $t$ is the total flow time (min), $Q$ is the volumetric flow rate (mL min$^{-1}$), $q_0$ is adsorption capacity (mg g$^{-1}$) and m is mass (g) of the adsorbent. The plot of $\ln(C_0/C_t - 1)$ vs. $t$ gives $K_{TH}$ and $q_0$. Selected Thomas parameters are given in Table 7.

$$\ln\left(\frac{C_t}{C_0-C_t}\right)=K_{YN}t-\tau K_{YN} \tag{15}$$

where τ is the time required for 50% adsorbate breakthrough (min), $t$ is the sample time (min), $K_{YN}$ in the rate constant(min$^{-1}$). $K_{YN}$ and τ were obtained by plotting $\ln(C_t/C_0 - C_t)$ vs. $t$. Selected parameters are given in Table 8.

$$\ln\left(\frac{C_t}{C_0}\right)=K_{AB}C_0t-K_{AB}N_0\frac{Z}{U_0} \tag{16}$$

where $C_0$, $C_t$ are influent and effluent concentration (mg L$^{-1}$) respectively, $K_{AB}$ kinetic constant (L mg$^{-1}$ min$^{-1}$) for Adams–Bohart model, $N_0$ is the saturation concentration (mg L$^{-1}$), $t$ is the flow time (min), $Z$ is the bed depth of the column (cm), $U_0$ is the superficial velocity (cm min$^{-1}$). The plot of $\ln(C_t/C_0)$ vs. $t$ gives the value of $K_{AB}$ and $N_0$ (Table 9).

Column data was fitted to the Thomas model to determine Thomas's rate constant and maximum adsorption capacity. As the input concentration was increased, $q_e$ was increased but $K_{TH}$ is decreased. The driving force for adsorption is the concentration difference between the solid and solution phases.

The column data were fitted with the Thomas model to determine the maximum solid-phase adsorption coefficient and Thomas rate constant $K_{TH}$. Values were obtained using nonlinear regression analysis. $R^2$ ranged from 0.991 to 0.999, indicating that the correlation of $C_t/C_0$ and $t$ is significant.

From Table 7, it is evident that the increasing concentration leads to an increase in Thomas constant but $q_0$

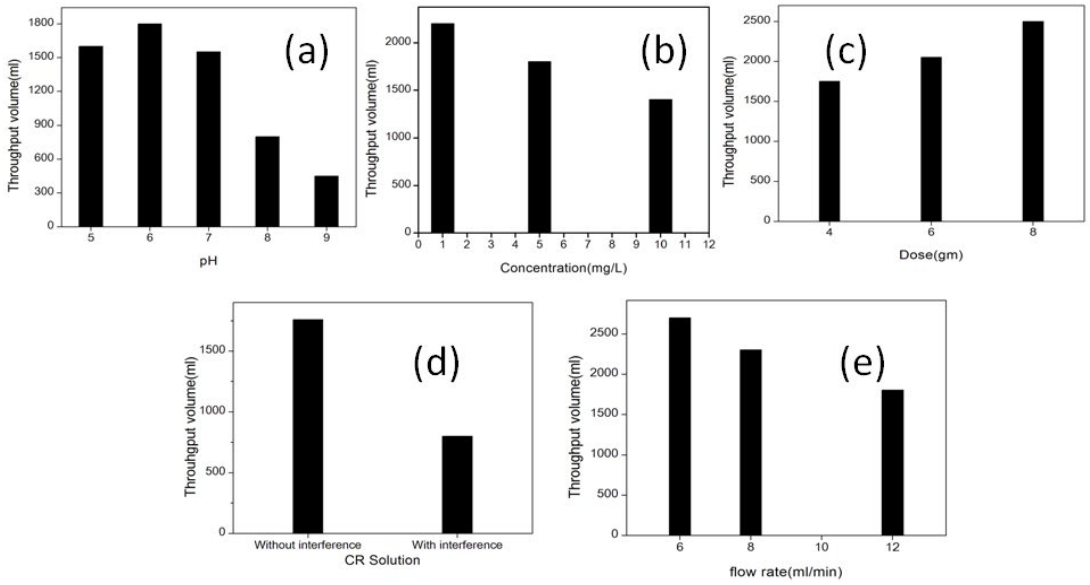


Fig. 11. Throughput volume passed of Congo red by IZO adsorbent (a) at different pH, (b) at different concentrations, (c) at a different dose, (d) at interference, and (e) effect of flow rate.

Table 4
Selected column parameters with varying pH

| Ph | $C_0$ (mg $L^{-1}$)[a] | Q (mL $min^{-1}$)[b] | Z(cm)[c] | Amount(g) | Bed volume[d] |
|---|---|---|---|---|---|
| 5 | 5 | 8 | 3 | 4 | 953 |
| 6 | 5 | 8 | 3 | 4 | 1,073 |
| 7 | 5 | 8 | 3 | 4 | 925 |
| 8 | 5 | 8 | 3 | 4 | 489 |
| 9 | 5 | 8 | 3 | 4 | 276 |

[a]Influent CR concentration, mg $L^{-1}$.
[b]volumetric flow rate, mL $min^{-1}$.
[c]Bed depth of column, cm.
[d]Bed volume (1 BV = $\pi r^2 h$ = 1.815 $cm^3$)

Table 5
Selected column parameters with varying input concentrations

| $C_0$ (mg $L^{-1}$)[a] | $Q$ (mL $min^{-1}$)[b] | Bed height $Z$ (cm)[c] | pH | Amount (g) | Bed volume[d] |
|---|---|---|---|---|---|
| 1 | 8 | 3 | 6 | 4 | 2,236 |
| 5 | 8 | 3 | 6 | 4 | 1,069 |
| 10 | 8 | 3 | 6 | 4 | 561 |

[a]Influent CR concentration, mg $L^{-1}$
[b]Volumetric flow rate, mL $min^{-1}$
[c]Bed depth of column, cm
[d]Bed volume (1 BV = $\pi r^2 h$)

Table 6
Selected parameters with varying dose and height

| pH | $C_0$ (mg $L^{-1}$)[a] | $Q$ (mL $min^{-1}$)[b] | $Z$ (cm)[c] | Amount (g) | Bed volume[d] |
|---|---|---|---|---|---|
| 6 | 5 | 8 | 3.2 | 4.25 | 964 |
| 6 | 5 | 8 | 4.8 | 6 | 744 |
| 6 | 5 | 8 | 6.3 | 8 | 716 |

[a]Influent CR concentration, mg $L^{-1}$
[b]Volumetric flow rate, mL $min^{-1}$
[c]Bed depth of column, cm
[d]Bed volume (1 BV = $\pi r^2 h$)

value decreases. This is due to the reason that the driving force for such adsorption is the concentration difference between the dye on the adsorbent surface and the dye in the solution.

When the bed height was increased from 3.2 to 6.3 cm, $q_0$ increased but $K_{TH}$ decreased. This was due to the higher contact time between the adsorbate and adsorbent.

When pH was raised from 5–9, $q_0$ value decreased while $K_{TH}$ value increased. This was due to the presence of the hydroxyl group in basic medium. When the flow rate increased, the adsorption capacity was increased, hence rate constant value decreased (Han et al. [66])

Yoon–Nelson model was applied to investigate the breakthrough behavior of CR on IZO. The rate constant value and time required for 50% CR breakthrough was obtained which is given in Table 8. With increasing flow rate, rate constant was found to increase and 50% breakthrough time (τ) was found to decrease. With bed height increasing, τ was found to increase with a decrease in rate constant $K_{YN}$.

The Adams Bohart adsorption model was applied to the data for the description of the initial part of the breakthrough curve. It gives the parameters maximum adsorption capacity ($N_0$) and kinetic rate constant ($K_{AB}$). The $K_{AB}$ value increased with the increase in the flow rate, but it decreased with bed depth and concentration. This means that the overall system kinetics was dominated by external mass transfer in the initial part of the adsorption [67].

### 3.9. Mechanism of adsorption

Adsorption studies provide information about the adsorption mechanism based on kinetics and isotherms studies [10]. The proposed mechanism is presented (Fig. 13). IZO contains a large number of hydroxyl moieties attached to metal centers. Below pH 7, the presence of protons makes the surface positively charged which favors hydrogen bonding and other weak interactions with the anionic dye molecule. Table 10 is shows the comparison of adsorption capacities of different dyes.

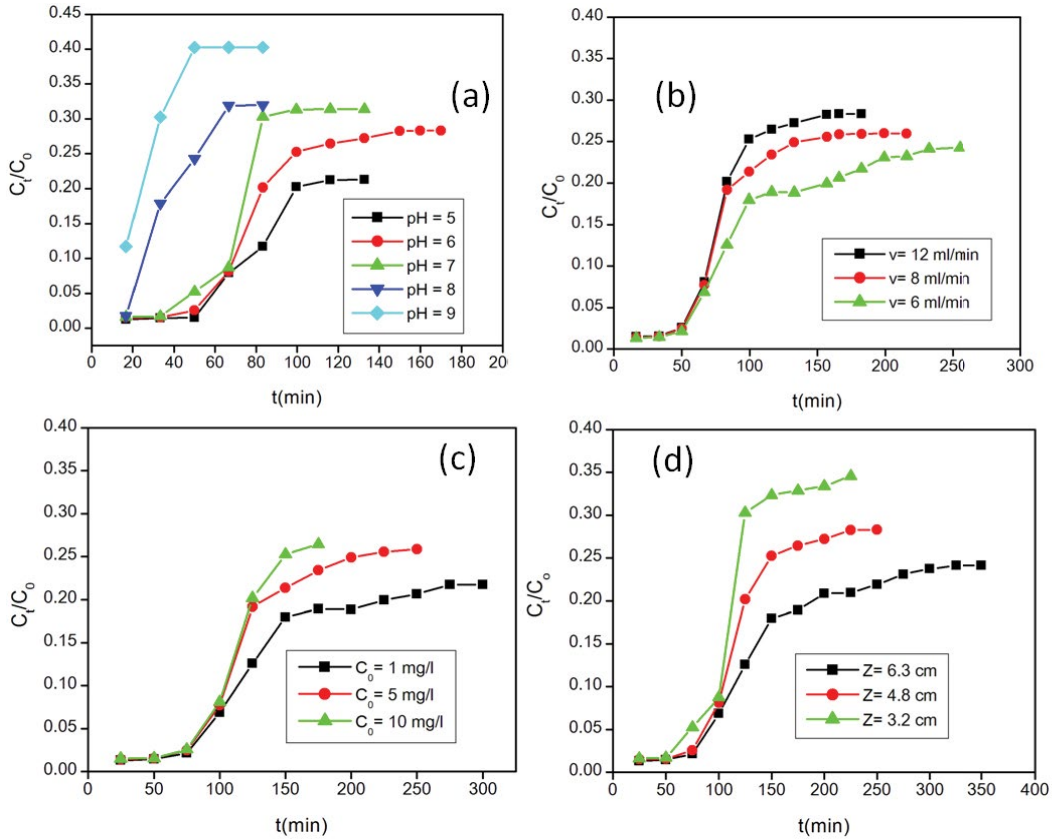


Fig. 12. Breakthrough curves: (a) effect of pH value on adsorption of CR, (b) effect of flow rate on adsorption of CR, (c) effect of concentration on adsorption of CR, and (d) effect of bed depth value on adsorption of CR.

Table 7
Thomas model parameters at different conditions using non-linear regression analysis

| Initial concentration (mg $L^{-1}$) $C_0$ | Bed height (cm) $Z$ | Flow rate mL $min^{-1}$ | pH | $K_{TH}$ (mL $min^{-1}$ $mg^{-1}$) | $q_0$ (mg $g^{-1}$) | $R^2$ |
|---|---|---|---|---|---|---|
| 5 | 3 | 8 | 5 | 0.251 | 52.12 | 0.970 |
| 5 | 3 | 8 | 6 | 0.188 | 72.88 | 0.995 |
| 5 | 3 | 8 | 7 | 0.138 | 101.29 | 0.978 |
| 5 | 3 | 8 | 8 | 0.189 | 76.67 | 0.988 |
| 5 | 3 | 8 | 9 | 0.191 | 41.23 | 0.999 |
| 5 | 3 | 6 | 6 | 0.196 | 69.51 | 0.993 |
| 5 | 3 | 8 | 6 | 0.188 | 72.88 | 0.995 |
| 5 | 3 | 12 | 6 | 0.163 | 99.46 | 0.991 |
| 1 | 3 | 8 | 6 | 0.175 | 79.46 | 0.995 |
| 5 | 3 | 8 | 6 | 0.189 | 72.89 | 0.995 |
| 10 | 3 | 8 | 6 | 0.190 | 71.72 | 0.994 |
| 5 | 3.2 | 8 | 6 | 0.179 | 78.98 | 0.994 |
| 5 | 4.8 | 8 | 6 | 0.121 | 121.28 | 0.996 |
| 5 | 6.3 | 8 | 6 | 0.105 | 156.56 | 0.994 |

## 4. Conclusions

Facile synthesis of iron zirconium binary oxide (IZO) was achieved by a controlled co-precipitation method in good yield. IZO was characterized by FTIR, SEM, powder XRD, Brunauer–Emmett–Teller surface area, TGA and $pH_{zpc}$. High surface area (200.307 $m^2$ $g^{-1}$) accounts for excellent dye adsorption. FTIR shows the presence of active –OH groups responsible for adsorption. SEM images show the presence of a porous surface. Powder XRD suggests the presence of

Table 8
Yoon–Nelson model parameters at different conditions using non-linear regression analysis

| Initial concentration (mg $L^{-1}$) $C_0$ | Bed height (cm) $Z$ | Flow rate mL $min^{-1}$ | pH | $K_{YN}$ ($min^{-1}$) | τ (min) | $R^2$ |
|---|---|---|---|---|---|---|
| 5 | 3 | 8 | 5 | 1.277 | 71.56 | 0.956 |
| 5 | 3 | 8 | 6 | 0.931 | 63.52 | 0.995 |
| 5 | 3 | 8 | 7 | 0.680 | 89.68 | 0.973 |
| 5 | 3 | 8 | 8 | 0.495 | 19.63 | 0.956 |
| 5 | 3 | 8 | 9 | 0.395 | 10.64 | 0.962 |
| 5 | 3 | 6 | 6 | 0.931 | 190.87 | 0.810 |
| 5 | 3 | 8 | 6 | 0.947 | 111.86 | 0.959 |
| 5 | 3 | 12 | 6 | 0.959 | 63.52 | 0.995 |
| 1 | 3 | 8 | 6 | 1.372 | 66.82 | 0.995 |
| 5 | 3 | 8 | 6 | 1.101 | 95.65 | 0.996 |
| 10 | 3 | 8 | 6 | 0.910 | 98.63 | 0.994 |
| 5 | 3.2 | 8 | 6 | 1.231 | 76.32 | 0.816 |
| 5 | 4.8 | 8 | 6 | 0.907 | 98.56 | 0.995 |
| 5 | 6.3 | 8 | 6 | 0.057 | 127.21 | 0.994 |

Table 9
Adams–Bohart parameters for CR at different conditions using non-linear regression analysis

| Initial concentration (mg $L^{-1}$) $C_0$ | Bed Height (cm) Z | Flow rate mL $min^{-1}$ | pH | $K_{AB}$(mL $min^{-1}$ $mg^{-1}$) | $N_0$(mg $L^{-1}$) | $R^2$ |
|---|---|---|---|---|---|---|
| 5 | 3 | 8 | 5 | 0.301 | 121.58 | 0.973 |
| 5 | 3 | 8 | 6 | 0.252 | 145.23 | 0.995 |
| 5 | 3 | 8 | 7 | 0.218 | 135.66 | 0.981 |
| 5 | 3 | 8 | 8 | 0.255 | 99.48 | 0.992 |
| 5 | 3 | 8 | 9 | 0.182 | 65.60 | 0.995 |
| 5 | 3 | 6 | 6 | 0.245 | 109.84 | 0.992 |
| 5 | 3 | 8 | 6 | 0.252 | 145.23 | 0.995 |
| 5 | 3 | 12 | 6 | 0.309 | 128.20 | 0.995 |
| 1 | 3 | 8 | 6 | 0.593 | 165.36 | 0.996 |
| 5 | 3 | 8 | 6 | 0.252 | 145.23 | 0.995 |
| 10 | 3 | 8 | 6 | 0.123 | 129.05 | 0.994 |
| 5 | 3.2 | 8 | 6 | 0.243 | 149.30 | 0.995 |
| 5 | 4.8 | 8 | 6 | 0.237 | 152.52 | 0.996 |
| 5 | 6.3 | 8 | 6 | 0.229 | 159.32 | 0.995 |

Table 10
Comparison of different adsorbent for various dyes

| Sl. No. | Adsorbent | Adsorbate | Efficiency (mg $g^{-1}$) | References |
|---|---|---|---|---|
| 1 | Chitosan-Lignin | Congo red | 76.92 | [4] |
| 2 | Graphene-carbon | Methylene blue | 65.70 | [6] |
| 3 | Chitosan-Lignin | Methylene blue | 36.25 | [27] |
| 4 | Cu(II)-AMTD xerogel | Methyl orange | 80 | [28] |
| 5 | Cu(II)-AMTD xerogel | Thymol blue | 96 | [28] |
| 6 | Cu(II)-AMTD xerogel | Acid fuchsine | 105 | [28] |
| 7 | IRA-938 resin | Rose bengal | 142.86 | [30] |
| 8 | $TiO_2$@AS | Methylene blue | 23.95 | [41] |
| 9 | $Fe_3O_4$/$ZrO_2$-CMCS | Sunset yellow | 143.2 | [46] |
| 10 | IZO | Congo red | 171 | Present work |

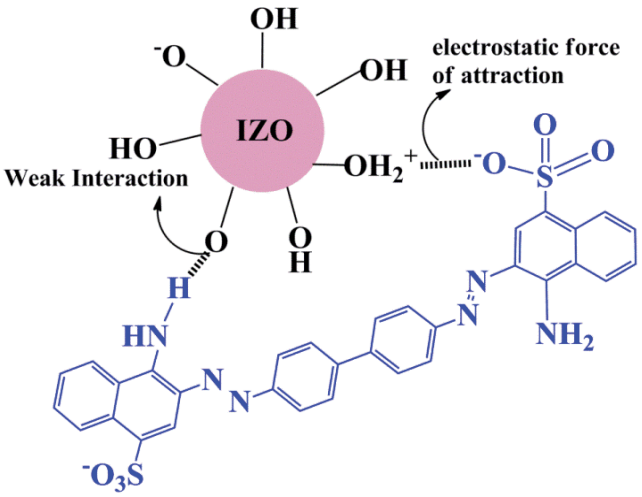


Fig. 13. Proposed mechanism of adsorption.

$Fe_2O_3$ and $ZrO_2$ units in the lattice. The surface charge was analyzed by the drift method and found to be neutral at 6.6 ($pH_{zpc}$ = 6.6). With an increase in pH, adsorption initially increases then decreases. The adsorption follows the pseudo-second-order rate and matches well with the Langmuir isotherm model. A negative value of enthalpy advocates for an exothermic process and negative free energy confirms spontaneity. The maximum adsorption capacity was estimated to be 171 mg $g^{-1}$. The material can be easily regenerated by dilute alkali solution and be reused up to five cycles without losing significant activities. Fixed bed column experiments under optimized conditions suggest promising field applicability of IZO. The breakthrough was analyzed with Thomas, Yoon–Nelson and Adams–Bohart models. Thomas and Adams–Bohart model was found the best fit for a breakthrough. It can be concluded that IZO is an efficient and promising low-cost adsorbent for the removal of CR from wastewater.

## Acknowledgment

J.M. thanks Central University of Jharkhand for fellowship. We gratefully acknowledge help from Dr. Shreya Bhattacharji (Department of English, Central University of Jharkhand) for English language editing.

## References

[1] J. Liu, H. Yong, S.N. Gosling, M. Kummu, M. Florke, S. Pfister, N. Hanasaki, Y. Wada, X. Zhang, C. Zheng, J. Alcamo, T. Oki, Water scarcity assessments in the past, present, and future, Earth's future, Adv. Earth Space Sci., 5 (2017) 545–559.
[2] M.T. Yagub, T.K. Sen, S. Afroze, H.M. Ang, Dye and its removal from aqueous solution by adsorption: a review, Adv. Colloid Interface Sci., 209 (2014) 172–184.
[3] R. Kumari, S. Dey, Facile removal of Congo red using Mahua (*Madhuca longifolia*) seeds, a low cost adsorbent, Int. J. Green Herb. Chem., 7 (2018) 237–250.
[4] V. Nair, A. Panigrahy, R. Vinu, Development of novel chitosan-lignin composites for adsorption of dyes and metal ions from wastewater,Chem. Eng. J., 254 (2014) 491–502.
[5] A. Kumar, G. Sharma, M. Naushad, P. Singh, S. Kalia, Polyacrylamide/$Ni_{0.02}Zn_{0.98}O$ nanocomposite with high solar light photocatalytic activity and efficient adsorption capacity for toxic dye removal, Ind. Eng. Chem. Res., 53 (2014) 15549–15560.
[6] F. Zhang, X. Chen, F. Wu, Y. Ji, High adsorption capability and selectivity of ZnO nanoparticles for dye removal, Colloids Surf., A, 509 (2016) 474–483.
[7] S. Wijannarong, S. Aroonsrimorakot, P. Thavipoke, A. Kumsopa, S. Sangjan, Removal of reactive dyes from textile dyeing industrial effluent by ozonation process, APCBEE Procedia, 5 (2013) 279–282.
[8] G. Mishra, M. Tripathy, A critical review of the treatment for decolorization of textile effluent, Colourage, 40 (1993) 35–38.
[9] J. Li, X. Wen, Q. Zhang, S. Ren, Adsorption and visible-light photo degradation of organic dyes with $TiO_2$/conjugated microporous polymer composites, RSC Adv., 8 (2018) 34560–34565.
[10] S. Rangabhashiyam, N. Anu, N. Selvaraju, Sequestration of dye from textile industry wastewater using agricultural waste products as adsorbents, J. Environ. Chem. Eng., 1 (2013) 629–641.
[11] S. Dawood, T.K. Sen, Removal of anionic dye Congo red from aqueous solution by raw pine and acid-treated pine cone powder as adsorbent: equilibrium, thermodynamic, kinetics, mechanism and process design, Water Res., 46 (2012) 1993–1946.
[12] T.S. Anirudhan, M. Ramachandran, Adsorptive removal of basic dyes from aqueous solutions by surfactant modified bentonite clay (organo clay): kinetic and competitive adsorption isotherm, Process Saf. Environ. Prot., 95 (2015) 215–225.
[13] M.L. Yola, T. Eren, N. Atar, S. Wang, Adsorptive and photocatalytic removal of reactive dyes by silver nanoparticle-colemanite ore waste, Chem. Eng. J., 242 (2014) 333–340.
[14] Y. Bulut, H. Aydın, A kinetics and thermodynamics study of methylene blue adsorption on wheat shells, Desalination, 194 (2006) 259–267.
[15] J. Fu, Q. Xin, X. Wu, Z. Chen, Y. Yan, S. Liu, Selective adsorption and separation of organic dyes from aqueous solution on polydopamine microspheres, J. Colloid Interface Sci., 461 (2016) 292–304.
[16] P. Egwuonwu, Adsorption of methyl red and methyl orange using different tree bark powder, Acad. Res. Int., 4 (2013) 2223–9944.
[17] A.M. Aljeboree, A.N. Alshirifi, A.F. Alkaim, Kinetic and equilibrium study for the adsorption of textile dyes on coconut shell activated carbon, Arabian J. Chem., 10 (2017) S3381–S3393.
[18] L. Liu, Z.Y. Gao, X.P. Su, X. Chen, L. Jiang, J.M. Yao, Adsorption removal of dyes from single and binary solutions using a cellulose-based bioadsorbent, ACS Sustainable Chem. Eng., 3 (2015) 432–442.
[19] E. Daneshvar, A. Vazirzadeh, A. Niazi, M. Kousha, Mu. Naushad, A. Bhatnagar, Desorption of methylene blue dye from brown macroalgae: effects of operating parameters, isotherm study and kinetic modelling, J. Cleaner Prod., 152 (2017) 443–453.
[20] A.A. Adeyemo, I.O. Adeoye, O.S. Bello, Adsorption of dyes using different types of clay: a review, Appl. Water Sci., 7 (2017) 543–568.
[21] T. Ngulube, J.R. Gumbo, V. Masindi, A. Maity, An update on synthetic dyes adsorption onto clay based minerals: a state-of-art review, J. Environ. Manage., 191 (2017) 35–57.
[22] A. Kausar, M. Iqbal, A. Javed, K. Aftab, Z. Nazli, H.N. Bhatti, S. Nouren, Dyes adsorption using clay and modified clay: a review, J. Mol. Liq., 256 (2018) 395–407.
[23] R. Yang, D. Li, A. Li, H. Yang, Adsorption properties and mechanisms of palygorskite for removal of various ionic dyes from water, Appl. Clay Sci., 151 (2018) 20–28.
[24] J.E. Aguiar, J.A. Cecilia, P.A.S. Tavares, D.C.S. Azevedo, E.R. Castellon, S.M.P. Lucena, I.J. Silva Junior, Adsorption study of reactive dyes onto porous clay heterostructures, Appl. Clay Sci., 135 (2017) 35–44.
[25] C. Puri, G. Sumana, Highly effective adsorption of crystal violet dye from contaminated water using graphene oxide intercalated montmorillonite nanocomposite, Appl. Clay Sci., 166 (2018) 102–112.
[26] Y. Wang, L. Zhu, X. Wang, W. Zheng, C. Hao, C. Jiang, J. Wu, Synthesis of aminated calcium lignosulfonate and its adsorption properties for azo dyes, J. Ind. Eng. Chem., 61 (2017) 321–330.

[27] A.B. Albadarin, M.N. Collins, Mu. Naushad, S. Shirazian, G. Walker, C. Mangwandi, Activated lignin-chitosan extruded blends for efficient adsorption of methylene blue, Chem. Eng. J., 307 (2017) 264–272.
[28] Y. Cheng, Q. Feng, X. Rena, M. Yina, Y. Zhou, Z. Xue, Adsorption and removal of sulfonic dyes from aqueous solution onto a coordination polymeric xerogel with amino groups, Colloids Surf., A, 485 (2015) 125–135.
[29] L. Wang, Z. Xu, Y. Fu, Y. Chen, Z. Pan, R. Wang, Z. Tan, Comparative analysis on adsorption properties and mechanisms of nitrate and phosphate by modified corn stalks, RSC Adv., 8 (2018) 36468–36476.
[30] M. Naushad, Z. Abdullah, A.L. Othman, M.R. Awual, S.M. Alfadul, T. Ahamad, Adsorption of rose bengal dye from aqueous solution by amberlite Ira-938 resin: kinetics, isotherms, and thermodynamic studies, Desal. Water Treat., 57 (2015) 13527–13533.
[31] Y. Hu, K. Li, Y. Li, H. Liu, M. Guo, X. Ye, Z. Wu, K. Lee, Dyes adsorption onto $Fe_3O_4$-bis(trimethoxysilylpropyl) amine composite particles: effects of pH and ionic strengthon electrostatic interactions, Chem. Select, 4 (2019) 617–622.
[32] K. Katsumata, K. Okada, Efficient method for adsorbing dye on $TiO_2$ electrodes in DSC production, Chem. Select, 2 (2017) 3060–3064.
[33] H. Jain, A. Joshi, C.N. Ramachandran, R. Kumar, Synthesis of a highly efficient multifunctional copper(II)-pyridyl complex for adsorption and photocatalytic degradation of organic dyes, Chem. Select, 4 (2019) 4952–4961.
[34] Z. Anfar, M. Zbair, H.A. Ahsaine, Y. Abdellaoui, A.A. El Fakir, El H. Amaterz, A. Jada, N. El Alem, Preparation and characterization of porous carbon@ZnO-NPs for organic compounds removal: classical adsorption versus ultrasound assisted adsorption, Chem. Select, 4 (2019) 4981–4994.
[35] A. Mohammad, S.N. Ansari, A. Chaudhary, K. Ahmad, R. Rajak, Md. Tauqeer, S.M. Mobin, Enthralling adsorption of different dye and metal contaminants from aqueous systems by cobalt/cobalt oxide nanocomposites derived from single-source molecular precursors, Chem. Select, 3 (2018) 5733–5741.
[36] D. Das, Structural diversity in hetero bimetallic complexes of alkaline earth metals and molybdenum, and selective dye adsorption properties of mixed metal oxides synthesized from the hetero bimetallic complexes, Chem. Select, 4 (2019) 1428–1436.
[37] S. Shanavas, A. Priyadharsan, K. Dharmaboopathi, I. Ragavan, C. Vidya, P.M. Anbarasan, Ultrasonically and photonically simulatable bi-ceria nanocubes for enhanced catalytic degradation of aqueous dyes: a detailed study on optimization, mechanism and stability,Chem. Select, 3 (2018) 12841–12853.
[38] C. Jiang, B. Fu, H. Cai, T. Cai, Efficient adsorptive removal of Congo red from aqueous solution by synthesized zeolitic imidazolate framework-8, Chem. Speciation Bioavailability, 28 (2016) 199–208.
[39] P. Wang, M. Cao, C. Wang, Y. Ao, J. Hou, J. Qian, Kinetics and thermodynamics of adsorption of methylene blue by a magnetic graphene-carbon nanotube composite, Appl. Surf. Sci., 290 (2014) 116–124.
[40] W.K. Jo, S. Kumar, M.A. Isaacs, A.F. Lee, S. Karthikeyan, Cobalt promoted $TiO_2$/GO for the photocatalytic degradation of oxytetracycline and Congo red, Appl. Catal., B, 201 (2017) 159–168.
[41] Y. Geng, J. Zhang, J. Zhou, J. Lei, Study on adsorption of methylene blue by a novelcomposite material of $TiO_2$ and alum sludge, RSC Adv., 8 (2018) 32799–32807.
[42] K. Kalpana, V. Selvaraj, Development of ZnS/SnS/A-FA nanorods at ambient temperature: binary catalyst for the removal of Congo red dye and pathogenic bacteria from wastewater, J. Ind. Eng. Chem., 41 (2016) 105–113.
[43] T.T.N. Phan, A.N. Nicolski, P.A. Bahri, D. Li, Adsorption and photo-Fenton catalytic degradation of organic dyes over crystalline $LaFeO_3$-doped porous silica, RSC Adv., 8 (2018) 36181–36190.
[44] J. Yang, D. Li, X. Wang, X.J. Yang, L.D. Lu, Rapid synthesis of nanocrystalline $TiO_2$/$SnO_2$ binary oxides and their photo induced decomposition of methyl orange, J. Solid State Chem., 165 (2002) 193–198.
[45] A.K. Arora, V.S. Jaswal, K. Singh, R. Singh, Metal/mixed metal oxides and their applications as adsorbents - a review, Int. J. Chem. Sci., 14 (2016) 3215–3227.
[46] T. Wu, Q. Shao, S. Ge, L. Bao, Q. Liu, The facile preparation of novel magnetic zirconia composites with the aid of carboxymethyl chitosan and their efficient removal of Dye, RSC Adv., 6 (2016) 58020–58027.
[47] D. Pathania, R. Katwal, G. Sharma, Fabrication, characterization and cytotoxicity of guar gum/copper oxide nanocomposite: efficient removal of organic pollutant, Mater. Sci. Forum, 842 (2016) 88–102.
[48] G. Sharma, S. Bhogal, V.K. Gupta, S. Agarwal, A. Kumar, D. Pathania, G.T. Mola, F.J. Stadler, Algal biochar reinforced trimetallic nanocomposite as adsorptional/photocatalyst for remediation of malachite green from aqueous medium, J. Mol. Liq., 275 (2019) 499–509.
[49] T. Tatarchuk, N. Paliychuk, R.B. Bitra, A. Shyichuk, Mu. Naushad, I. Mironyuk, D. Ziolkowska, Adsorptive removal of toxic methylene blue and acid orange 7 dyes from aqueous medium using cobalt-zinc ferrite nanoadsorbents, Desal. Water Treat., 150 (2019) 374–385.
[50] T. Tatarchuk, N. Paliychuk, M. Pacia, W. Kaspera, W. Macyk, A. Kotarba, B.F. Bogacz, A.T. Pedziwiatr, I. Mironyuk, R. Gargula, P. Kurzydło, A. Shyichuk, Structure-redox reactivity relationships in $Co_{1x}Zn_3Fe_2O_4$: the role of stoichiometry, New J. Chem., 43 (2019) 3038–3049.
[51] G. George, M.P. Saravanakumar, Facile synthesis of carbon-coated layered double hydroxide and its comparative characterisation with Zn–Al LDH: application on crystal violet and malachite green dye adsorption—isotherm, kinetics and Box-Behnken design, Environ. Sci. Pollut. Res., 25 (2018) 30236–30254.
[52] K. Karthik, M. Shashank, V. Revathi, T. Tatarchuk, Facile microwave-assisted green synthesis of NiO nanoparticles from *Andrographispaniculata* leaf extract and evaluation of their photocatalytic and anticancer activities, Mol. Cryst. Liq. Cryst., 673 (2018) 70–80.
[53] I. Mironyuk, T. Tatarchuk, H. Vasylyeva, V.M. Gun'ko, I. Mykytyn, Effects of chemosorbed arsenate groups on the mesoporous titania morphology and enhanced adsorption properties towards Sr(II) cations, J. Mol. Liq., 282 (2019) 587–597.
[54] I. Mironyuk, T. Tatarchuk, Mu. Naushad, H. Vasylyeva, I. Mykytyn, Highly efficient adsorption of strontium ions by carbonated mesoporous $TiO_2$, J. Mol. Liq., 285 (2019) 742–753.
[55] I.F. Mironyuk, V.M. Gun'ko, H.V. Vasylyeva, O.V. Goncharuk, T.R. Tatarchuk, V.I. Mandzyuk, N.A. Bezruka, T.V. Dmytrotsa, Effects of enhanced clusterization of water at a surface of partially silylated nanosilica on adsorption of cations and anions from aqueous media, Microporous Mesoporous Mater., 277 (2019) 95–104.
[56] D. Pathania, Sarita, P. Singh, S. Pathania, Preparation and characterization of nanoscalecadmium oxide using bovine serum albumin as green capping agent and its photocatalytic activity, Desal. Water Treat., 52 (2014) 3497–3503.
[57] R. Kumari, S. Dey, Synthesis of porous iron-zirconium mixed oxide fabricated ethylene diamine composite for removal of cationic dye, Desal. Water Treat., 154 (2019) 319–329.
[58] S. Chawla, H. Uppal, M. Yadav, N. Bahadur, N. Singh, Zinc peroxide nanomaterial as an adsorbent for removal of Congo red dye from wastewater, Ecotoxicol. Environ. Saf., 135 (2017) 68–74.
[59] A.A. Alqadami, Mu. Naushad, M.A. Abdalla, M.R. Khan, Z.A. Alothman, Adsorptive removal of toxic dye using $Fe_3O_4$–TSC nanocomposite: equilibrium, kinetic, and thermodynamic studies, J. Chem. Eng. Data, 61 (2016) 3806–3813.
[60] A. Lassoued, B. Dkhil, A. Gadri, S. Ammar, Control of the shape and size of iron oxide (a-$Fe_2O_3$) nanoparticlessynthesized through the chemical precipitation method, Results Phys., 7 (2017) 3007–3015.
[61] V.S. Mane, P.V.V. Babu,Studies on the adsorption of brilliant green dye from aqueous solution onto low-cost NaOH treated saw dust, Desalination, 273 (2011) 321–329.

[62] R. Han, Y. Wang, W. Yu, W. Zou, J. Shi, H. Liu, Biosorption of methylene blue from aqueous solution by rice husk in a fixed-bed column, J. Hazard. Mater., 141 (2007) 713–718.
[63] R. Kumari, S. Dey, A breakthrough column study for removal of malachite green using coco-peat, Int. J. Phytorem., 21 (2019) 1263–1271.
[64] S. Rouf, M. Nagapadma, Modeling of fixed bed column studies for adsorption of azo dye on chitosan impregnated with a cationic surfactant, Int. J. Sci. Eng. Res., 6 (2015) 538–545.
[65] S. Biswas, U. Mishra, Continuous fixed-bed column study and adsorption modeling: removal of lead ion from aqueous solution by charcoal originated from chemical carbonization of rubber wood sawdust, J. Chem., 2015 (2015) 1–9, http://dx.doi.org/10.1155/2015/907379.
[66] R. Han, Y. Wang, X. Zhao, Y. Wang, F. Xie, J. Cheng, M. Tang, Adsorption of methylene blue by phoenix tree leaf powder in a fixed-bed column: experiments and prediction of breakthrough curves, Desalination, 245 (2009) 284–297.
[67] Z. Aksu, F. Gonen, Biosorption of phenol by immobilized activated sludge in a continuous packed bed: prediction of breakthrough curves, Process Biochem., 39 (2004) 599–613.